Non-descanned multifocal multiphoton microscopy with a multianode photomultiplier tube

Jae Won Cha,[1] Elijah Y. S. Yew,[1] Daekeun Kim,[2] Jaichandar Subramanian,[3] Elly Nedivi,[3,4] and Peter T. C. So[1,5]
[1]*Department of Mechanical Engineering, Massachusetts Institute of Technology, Cambridge, MA, USA*
[2]*Department of Mechanical Engineering, Dankook University, Korea*
[3]*Picower Institute for Learning and Memory, Massachusetts Institute of Technology, Cambridge, MA, USA*
[4]*Departments of Brain and Cognitive Sciences, and Biology, Massachusetts Institute of Technology, Cambridge, MA, USA*
[5]*Department of Biological Engineering, Massachusetts Institute of Technology, Cambridge, MA, USA*

(Received 9 September 2014; accepted 28 September 2014; published online 23 March 2015)

Multifocal multiphoton microscopy (MMM) improves imaging speed over a point scanning approach by parallelizing the excitation process. Early versions of MMM relied on imaging detectors to record emission signals from multiple foci simultaneously. For many turbid biological specimens, the scattering of emission photons results in blurred images and degrades the signal-to-noise ratio (SNR). We have recently demonstrated that a multianode photomultiplier tube (MAPMT) placed in a descanned configuration can effectively collect scattered emission photons from each focus into their corresponding anodes significantly improving image SNR for highly scattering specimens. Unfortunately, a descanned MMM has a longer detection path resulting in substantial emission photon loss. Optical design constraints in a descanned geometry further results in significant optical aberrations especially for large field-of-view (FOV), high NA objectives. Here, we introduce a non-descanned MMM based on MAPMT that substantially overcomes most of these drawbacks. We show that we improve signal efficiency up to fourfold with limited image SNR degradation due to scattered emission photons. The excitation foci can also be spaced wider to cover the full FOV of the objective with minimal aberrations. The performance of this system is demonstrated by imaging interneuron morphological structures deep in the brains of living mice. [http://dx.doi.org/10.1063/1.4916040]

I. INTRODUCTION

Multiphoton excitation fluorescence microscopy has inherent 3D resolution due to the nonlinear dependence of excitation efficiency on the incident light flux distribution.[1,2] Multiphoton excitation can be localized to a femtoliter region at the focal point of a high numerical aperture objective. This microscope modality has become one of the most common solutions for non-invasive, deep imaging in many turbid biological specimens. Improving multiphoton microscope imaging speed is important for many research areas. An example is in the studies of fast intra- and inter-cellular signaling events, such as monitoring voltage or calcium signals. Another example involves animal studies where motion artifacts and length of anesthesia should be limited. Several methods have been developed to improve imaging speed beyond conventional point scanning systems based on galvanometric mirror scanners. One approach uses higher speed scanners such as polygonal mirrors,[3] resonant mirror scanners,[4] or acousto-optical deflectors.[5–8] These high speed scanners can typically achieve frame rates up to about 1 kHz in tissues with an imaging depth comparable to conventional multiphoton microscopy. However, the higher speed scanning requires

a correspondingly decreased pixel dwell time resulting in poorer signal-to-noise ratio (SNR). This tradeoff can be partially compensated by increasing the excitation laser power but laser power is ultimately limited by specimen photodamage and excitation saturation.[9,10] Another approach is two-photon wide-field imaging based on temporal focusing.[11,12] In this case, two-photon excitation is localized to a plane, instead of a point, by controlling the spectral dispersion of the ultrafast light pulse at different distances from the focal plane. However, wide-field two-photon imaging is often limited by the lower axial resolution and the smaller field-of-view (FOV) due to the need for much higher peak power laser pulses. Another popular approach to improve imaging speed is multifocal multiphoton microscopy (MMM).[13,14] With a lenslet array or a diffractive optical element (DOE),[15,16] multiple foci are generated and scanned simultaneously. Within the limit of available laser power, about 100 foci can be effectively generated with a standard Ti-Sapphire oscillator resulting in an improvement in imaging speed of approximately two orders of magnitude. For MMM systems, simultaneous acquisition of data from many foci often require the use of an area detector, such as a CCD or a CMOS sensor.[13,14] Spatial registration is achieved by telecentric mapping of the specimen plane on to the image sensor plane. In a turbid specimen, the emission photons are scattered resulting in image blurring. More importantly, as scattered emission photons are scattered away from the correct location, they contribute to an increased background and degrade image SNR. To overcome this limit of emission light scattering, MMM using a multianode photomultiplier tube (MAPMT) in a descanned detection configuration has been developed.[17,18] As in most confocal microscopes, the descanned geometry guides the emission photons from each focus backward along the same optical path shared with the excitation beams. Since the motion of the scanning mirror is much slower than the speed of light, the emission light rays after the scanning mirror become stationary in relation to scanner motion and can be separated from the excitation beams with a dichroic mirror. The unscattered ballistic emission photons generated by each focus are focused at the cathode which is correspondingly located at the center of each anode of the MAPMT. This approach is described as "descanned" detection. While the scattered emission photons may not be focused at the center of the anode, much of the scattered photons can still be collected effectively by the appropriate anode. Intuitively, a larger area projected by each anode at the specimen plane will result in greater collection efficiency of these scattered emission photons. At the limit of an infinitely large anode, the collection efficiency of scattered emission photons will be comparable to that of single point focusing multiphoton system. Since the infinitely large anode limit cannot be realized, if the sample is highly scattering and imaging depth is large, the scattered emission photons will reach neighboring anodes. This effect results in the presence of 'ghost' images in the neighboring sub-images. We have shown that a number of post-processing algorithms can be developed to reassign the scattered photons into the neighboring pixels and mostly eliminate these ghost images.[17] However, it is always better to minimize the deleterious effect of the scattering of emission photons by using a high numerical aperture (NA), low magnification objective so that the foci can be physically separated as far as possible over the FOV of the specimen plane. Today, the most advanced objectives for multiphoton imaging typically has NA on the order of 1.0 and FOV of about 1 mm. This large FOV presents significant challenges in the design of the intermediate optics for MMM. The edge foci are generated from rays that subtend large angles with the optical axis and are far from paraxial, and significant aberration can result from the use of intermediate optics with low f-numbers. This challenge is compounded by the fact that the excitation beams must first be de-magnified to fit onto the millimeter size galvanometric scan mirrors as their small size and light weight are important for fast scanning. The excitation beams must be magnified again to backfill the several centimeter diameter back aperture of these large FOV objectives to ensure diffraction limited focusing. These beam size control requirements are difficult to satisfy using commercially available high f-number lenses that have short focal distances. These short focal distance lenses make it difficult to accommodate components with substantial physical sizes, such as the galvanometric scanning mirrors, in the optical path. The need for some low f-number lenses results in an aberrated point spread function (PSF), especially at the edge and corner foci and leads to resolution and signal strength degradation at the edges of the image. Another major problem of the descanned MMM design is the loss of the emission signals in the descanned detection configuration that has many more optical surfaces resulting in the attenuation of both scattered and unscattered emission

photons. The much longer optical path further results in loss of a majority of the scattered emission photons that are often scattered at large angles relative to the optical axis. As such, signal attenuation in the descanned geometry can become quite severe.[17] This problem is, of course, well known in point scanning multiphoton microscope and the preferred method to overcome this limitation is to use a non-descanned configuration.[19,20] In this work, we propose a novel non-descanned MMM with a MAPMT detector that preserves the SNR immunity to scattered emission photon scattering but allows scanning over millimeter scale FOV with minimal aberration and improves the collection of emission photons by up to four times.

II. METHOD

A. Non-descanned MMM with an imaging detector

Figure 1 shows the system configuration of a non-descanned MMM with an imaging detector similar to previous publications.[13,14] The light source is a Chameleon Ultra II (Coherent, Santa Clara, CA). The excitation laser beam is split into a number of beamlets with a DOE (customized, 8×8 for 780 nm and 4×4 for 910 nm, Holo/Or, Rehovoth, Israel). The multiple beamlets are sent to x-y galvanometric mirror scanners (6215H, Cambridge Technology, Lexington, MA), and scanned simultaneously. The scanned beamlets are expanded to overfill the back aperture of a 20× water immersion objective lens (W Plan-Apochromat, 1.0 NA, Zeiss, Thornwood, NY) with different entrance angles. The objective lens generates an array of excitation foci on the focal plane in a specimen. The emission photons are collected by the same objective lens. In the very early design of MMM the emission photons pass through the dichroic mirror after the objective lens according to the separation wavelength, and arrive at an imaging detector, such as a CCD camera. The camera acquires all the emission photons until scanning is done. As discussed, this configuration is very susceptible to SNR loss due to the scattering of emission photons.

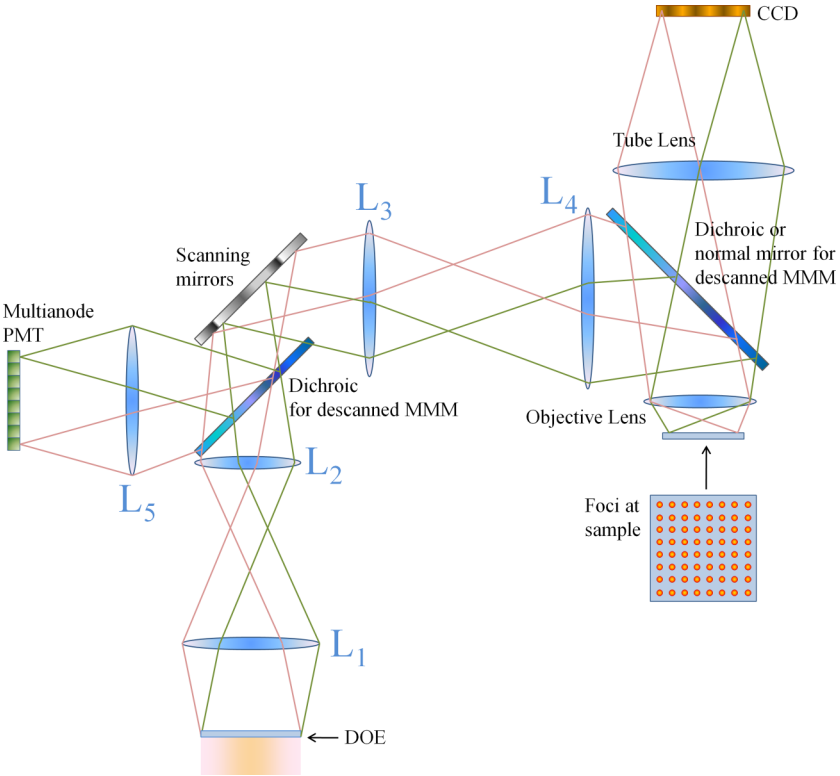

FIG. 1. The schematic of an older generation MMM. Two generations of MMM are implemented here including a non-descanned MMM acquiring signal with a camera and a descanned version acquiring signal with a MAPMT.

B. Descanned MMM with a MAPMT

Figure 1 also shows the descanned detection configuration with a MAPMT. For descanning, the dichroic mirror between the objective lens and lens L_4 is replaced by a normal mirror, and the dichroic mirror is located between the scanning mirrors and lens L_2. The emission photons from the sample travel backward through the optical path shared with the excitation beam. After the scanning mirrors the beams of the emission photons become stationary, independent of scanner position; this process is called "de-scanning" and is well known in the design of confocal microscopes.[21–24] De-scanning is possible because the transit time of the excitation photon, the fluorescence lifetime, and the arrival time of the emission photons in combination is much faster than the motion of the scanner and the scanner is virtually motionless relative to the light. The symmetry of the light path between excitation and emission light rays ensures that the emission rays directions are constant independent of scanner motion. The stationary emission rays from the foci are reflected by the dichroic mirror (Chroma Technology, Bellows Falls, VT) and focused at cathode locations that correspond to the centers of each of the anodes of the MAPMT (H7546B-20, Hamamatsu, Bridgewater, NJ). An IR blocking filter (BG39, Chroma Technology, Bellows Falls, VT) and a short-pass filter (ET680sp-2p, Chroma Technology, Bellows Falls, VT) are installed before the MAPMT to block the excitation light. As long as the anode surface corresponds to a sufficiently large area on the specimen plane, we can ensure that most of the scattered emission photons are collected in the designated channels. Therefore, the use of de-scanning and the MAPMT detector can suppress the scattering of emission photons, resulting in higher SNR. However, as described above, there is significant loss of the emission signal due to the many optical surfaces and the long descanning path with limited size of optics (e.g. scanning mirrors). Significant aberration of edge foci is also observed with high NA, large FOV objectives.

C. Non-descanned MMM with a MAPMT

The use of a high NA, large FOV objective allows excitation to be spaced far apart in the specimen plane minimizing crosstalk between the emission signals from neighboring foci. Unfortunately, the aberrations from the intermediate optics prohibit fully utilizing the FOV of the objective lens in the descanned configuration. In Fig. 1, after the DOE, the size of the multiple excitation beamlets must be decreased with lens L_1 (f 300 mm, singlet, KPX232AR.16, Newport, Irvine, CA) and lens L_2 (f 75 mm, doublet, AC508-075-B-ML, Thorlabs, Newton, NJ) in a 4-f geometry to fit onto small, 5 mm size scanning mirrors (6215H, Cambridge Technology, Lexington, MA) to allow fast mechanical scanning. The L_3 (f 35 mm, doublet, AC254-035-B-ML, Thorlabs, Newton, NJ) and L_4 (f 175 mm, singlet, KPX196AR.16, Newport, Irvine, CA) lenses in another 4-f configuration then expand the beamlets to slightly overfill the 2 cm diameter back aperture of the objective lens ensuring diffraction limited focusing. Given the finite physical size of the scanning mirror assembly, lenses L_2 and L_3 must have sufficiently long focal lengths and relative poor (low) f-numbers, thus generating large aberrations especially for edge and corner foci. Consequently, the final FOV becomes very limited (only around 300 μm × 300 μm from the available size of 700 μm × 700 μm). Large size scanning mirrors are available to avoid the aberrations from the reduction and the expansion processes, but scanning with them is slow. In addition, the use of larger mirrors also results in larger physical separation between the x-axis scanning mirror and y-axis scanning mirror resulting in greater non-uniformity of excitation over the FOV.[25]

Figure 2 shows the schematic of the new, non-descanned MMM with MAPMT. The scanning mirrors are positioned before the DOE. In this configuration the excitation beam can be expanded gradually with two 4-f beam expanders corresponding to lens pairs of L_1 (Eyepiece E-PL 10x/20, Zeiss, Thornwood, NY) and L_2 (f 100 mm, doublet, AC508-100-B-ML, Thorlabs, Newton, NJ), and L_3 (f 200 mm, doublet, AC508-200-B-ML, Thorlabs, Newton, NJ) and L_4 (f 300 mm, singlet, KPX232AR.16, Newport, Irvine, CA). This arrangement improves the overall f-numbers of the intermediate optics and minimizes the aberrations. After the lens L_2, the scanned laser beam enters the DOE with various angles of incidence (AOI). Within a small range of AOI (in our design ±0.4 °), the performance of the DOE was consistent. The dichroic mirror is located at the mirror

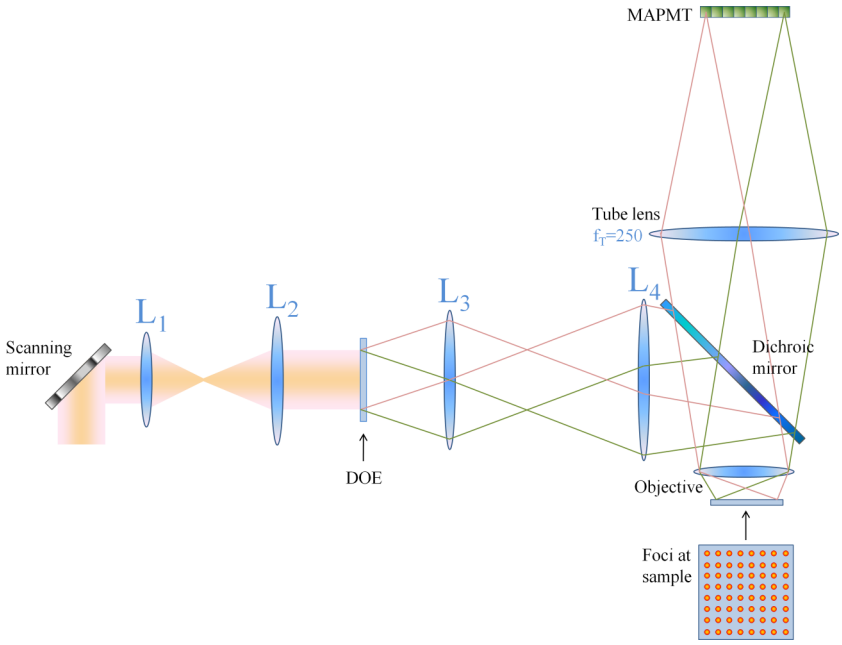

FIG. 2. The schematic of MMM system with non-descanned detection.

position between lens L_4 and the objective lens so that the emission photons reach the MAPMT with a shorter path length (500 mm versus 872 mm of the descanned configuration in Fig 1). The same IR blocking filter (BG39, Chroma Technology, Bellows Falls, VT) and the short-pass filter (ET680sp-2p, Chroma Technology, Bellows Falls, VT) are installed before the MAPMT to block the excitation light. Figure 3 shows the f-numbers of our two MMM systems optimized for each descanned and non-descanned case using commercially available lenses.

The four lenses in each case were optimized to utilize the full FOV of the 20× objective lens (FOV: 1 mm diameter at a sample plane), which provides about 700 μm × 700 μm scanning area. The lenses that have lower f-numbers generate dominant aberrations for the final PSF at the sample plane. Generally, if the f-number is smaller than 10, a doublet or more complex compound lens should be used, instead of a singlet, to minimize aberrations.[26,27] The descanned MMM design contains two low f-number doublet lenses before and after the scanning mirrors (L_2 and L_3), but their f-numbers improves from about 2 in the descanned configuration to over 5 in the non-descanned configuration. The f-number of the lens L_1 is slightly decreased, but it is a theta lens that can be normally used as a scan lens and can afford a slightly lower f-number of 5.9.

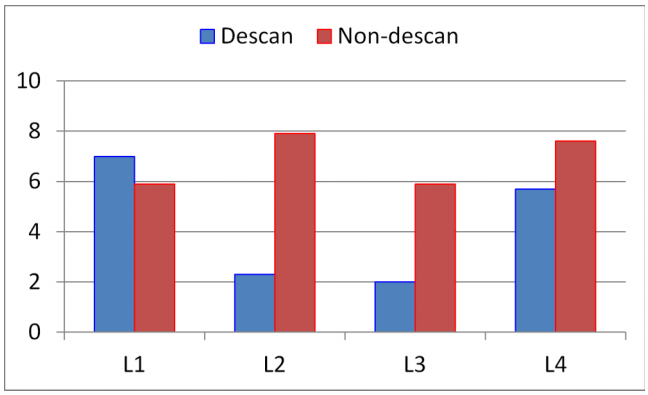

FIG. 3. The f-numbers of Lens L1, L2, L3, and L4 in the descanned and non-descanned MMM.

D. ZEMAX simulation for the corner and edge foci of the non-descanned MMM

As discussed above, the non-descanned MMM geometry can avoid low f-numbers optics resulting in less aberration. Using the optical system design software, ZEMAX (Radiant ZEMAX LLC, Bellevue, WA) the aberration coefficients were calculated and spot diagrams were simulated.

With the improved aberration coefficients, the RMS radius of the simulated corner focus became smaller by a factor of 3. The bottom two rows of Fig. 4 show the actual focus images taken by a camera at the MAPMT location of Fig. 2. It is visually shown that the second corner focus and edge focus were improved. The middle plots show the normalized PSF profiles of the displayed actual foci, and the improvement was up to two-fold. For more effective comparison, the first corner foci should have been compared, but they could not be imaged due to beam clipping at lens L3 of the descanned MMM (Fig. 1) since there was no available commercial lens with sufficient diameter at the designed focal length. It should be noted that the camera image of these foci are different from the 2D PSF calculation since signals for the camera are integrated axially over the 3D volume.

E. Detection strategy: image shifting

The non-descanned MMM is expected to achieve a larger FOV with improved PSF. However, in the non-descanned geometry, the emission photons from the n × n excitation foci are no longer

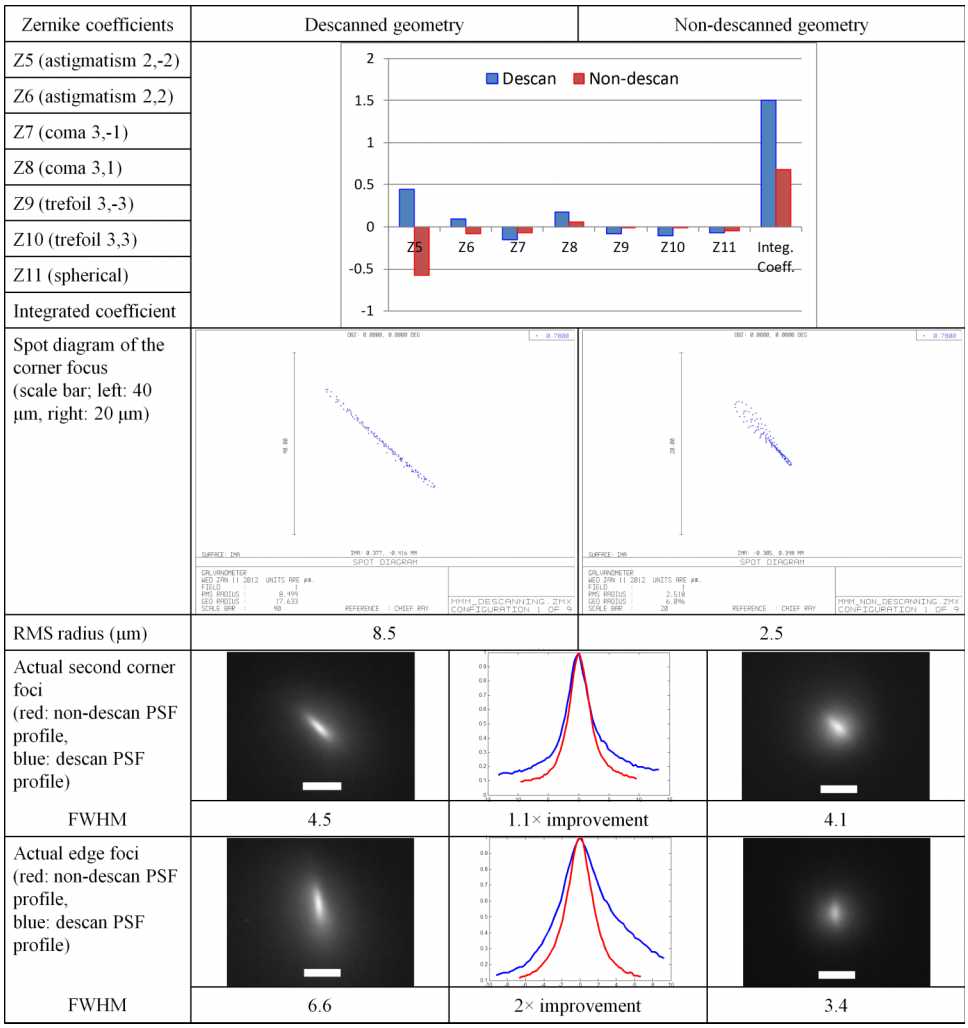

FIG. 4. The ZEMAX simulation of the excitation foci in the descanned and non-descanned geometry, and their actual images. The scale bars in the actual images are 5 μm long.

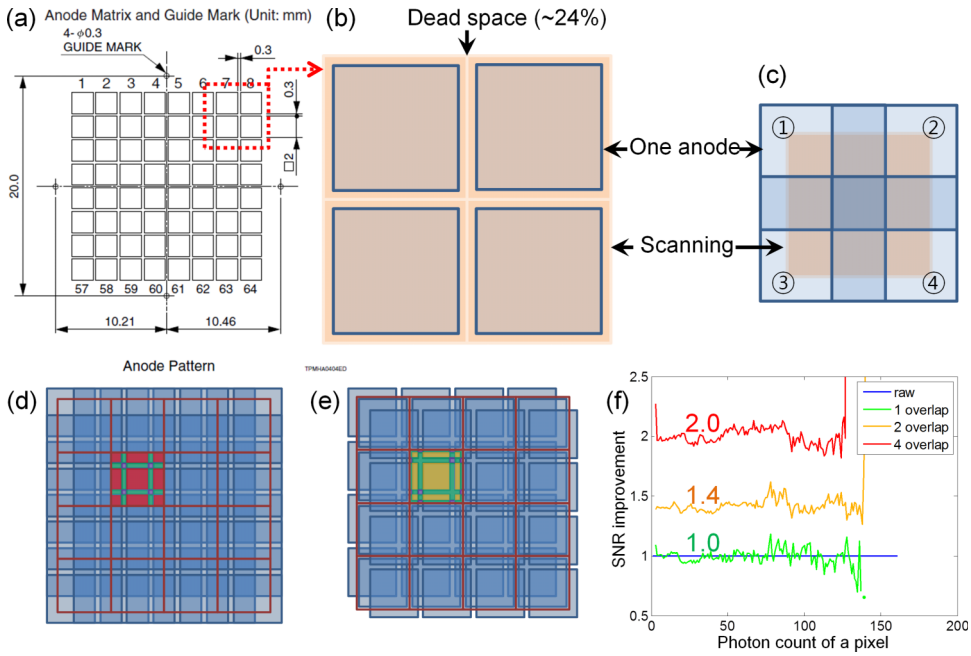

FIG. 5. The detection scheme of the sample shift. (a) The anode matrix of the MAPMT with 0.3 mm dead spaces.[28] (b) The scan areas in a specimen (orange) and the areas covered by the anodes (blue). (c) One scan area covered by 4 time sample shift. (d) Overlapped scan areas with 4 time and (e) 3 time movement in the 4 × 4 MMM case. Red: 4 time, yellow: 3 time, green: 2 time, and violet: 1 time overlap. (f) SNR improvement of each case.

stationary at the cathode surface of the MAPMT. Since there are dead spaces between anodes in the MAPMT, the direct telecentric mapping of the emission photons onto the MAPMT results in a loss of information when the foci are incident on the dead space during scanning (Fig 5(a)). To avoid the dead spaces of the MAPMT, we demonstrate a detection scheme that involves shifting the specimen and acquiring multiple exposures. Consider a portion of the image (a sub-image) corresponding to the surface area of four neighboring anodes (Fig. 5(b)). By moving the specimen four times, each quadrant of the sub-image can be collected by the center area of each anode avoiding the dead space (Fig 5(c) and 5(d)). In addition, when the emission focus is close to the edge of the anode of the MAPMT in one acquisition, another acquisition can collect the same emission photons close to the center of its anode providing the information for the emission photon reassignment to minimize the crosstalk between anodes. The minimal number of sample shifts required to cover the dead spaces is three (Fig 5(e)), but a four-step movement is preferable to better utilize the center area of each anode where there is less aberration and to ensure more uniform SNR across the final image when the individual captures are synthesized. In our implementation, the specimens were translated manually by a custom-built stage. While our stage is currently slow with movement time of a few seconds, the time required for producing the 42.5 μm shift can be accomplished with a commercial high performance stage within a couple of milliseconds. We kept a constant pixel dwell time of 40 μs for both single focus scanning experiment and the descanned MMM experiment. The total data acquisition time was $4/n^2$ shorter than single focus scanning assuming that n × n foci are used. With this approach, the image acquired 4 times more photons with the exception of the small dead spaces where signal either did not increase or only doubled (Fig 5(d)-5(e)). The four times higher signals result in two times higher SNR according to Poisson noise statistics. The SNR dependences in different regions of the image can be seen from imaging a 300 μM fluorescein solution (Fig 5(f)). However, it should be noted that we can, in principle, keep SNR the same and shorten the acquisition time by 4 and still maintain a speed gain of n^2 for n × n foci.

III. RESULTS

A. Fluorescent beads images with 8 × 8 MMM

To demonstrate the capability of this non-descanned MMM, we first imaged a fluorescent bead sample. The sample was prepared with 4 μm diameter fluorescent polystyrene microspheres (F8859, Molecular Probes, Eugene, OR) immobilized in 3D by a 2 % agarose gel (UltraPure Low Melting Point Agarose, Invitrogen, Carlsbad, CA). To mimic the scattering characteristic of typical tissue specimens, a 2 % fat emulsion (Microlipid, Nestle, Vevey, Switzerland) was added to the sample.[29,30] The excitation wavelength was 780 nm, and the laser power per focus was adjusted according to the imaging depth to maximize signal with no excitation satuarion (2.5 mW and 5 mW for 40 μm and 80 μm depth respectively in the non-descanned MMM case, and 15 mW for the single focus scanning case). The dwell time was 40 μs for both cases. The scanning area of one focus in the non-descanned MMM was 85 μm × 85 μm with 0.4 μm resolution and the whole FOV was 680 μm × 680 μm with imaged 8 × 8 foci. As described in section II E, the sample was imaged four times with 42.5 μm x and y shifts, and the four images were integrated to one final image. The single focus image was scanned with the same resolution (0.4 μm) over a FOV of 410 μm × 410 μm (1024 × 1024 pixels). Cropped images acquired with either method are displayed in Fig 6 for better presentation of the 4 μm beads. The acquired raw images are typically not uniform (the center area is brighter than the edge area) because while the x and y scanning mirrors are closely spaced, they cannot be both at the eye-point of the scanning system. Further, there were aberrations due to the large FOV. In addition, the emission signal of the non-descanned MMM is focused and scanned on the cathod surface of the MAPMT, so the acquired image contains the physical pattern of the cathode. To avoid the non-uniformity in the raw images, they were normalized with a 20 times averaged (minimal shot noise) image of a 300 μM uniform fluorescein solution.

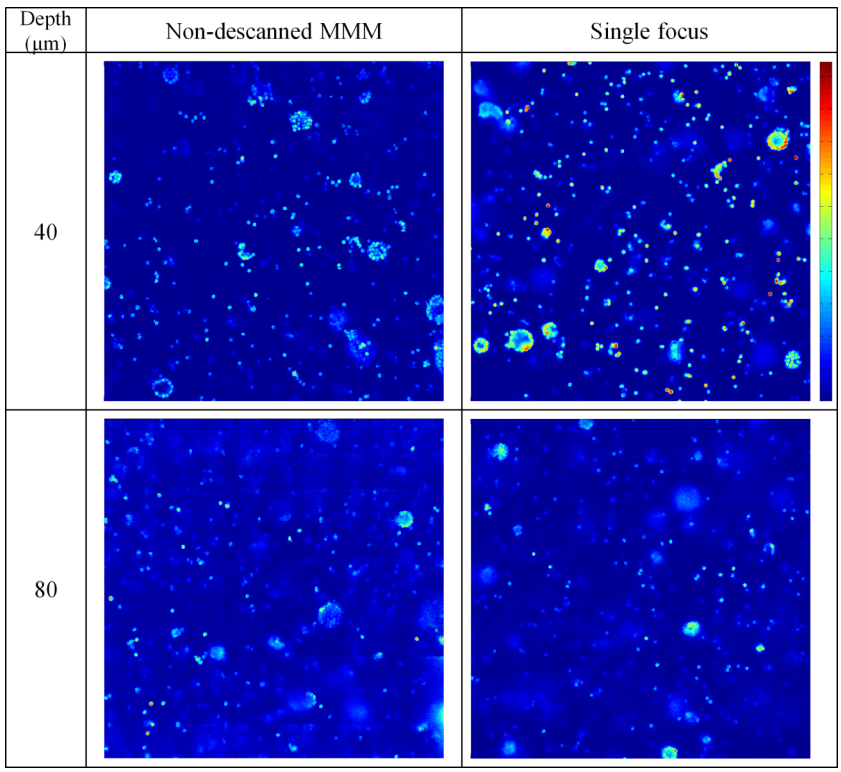

FIG. 6. Fluorescent bead images in the non-descanned MMM and the standard single focus scanning microscope at 40, and 80 μm imaging depths. The images are 410 μm × 410 μm with 0.4 μm resolution.

Figure 6 shows that the non-descanned MMM can successfully image the bead sample. The measured full-width at half-maximum (FWHM) of the bead were the same, 4.1 μm at 40 μm depth, and 4.2 and 4.1 μm at 80 μm depth, for the non-descanned MMM and the single focus scanning images. Thus, the non-descanned MMM shows comparable imaging capabilities to the single focus scanning, but is 16 times faster (excluding the four time manual movement of the sample). For further verification we investigated the capability of large FOV imaging and compared the emission signal loss between the descanned and non-descanned MMM

B. Field-of-view comparison

To compare the FOV of the descanned and non-descanned MMM, the same sample was imaged in both systems. The sample was a mouse kidney section labeled with three fluorescent dyes (FluoCells® Prepared Slide #3, F24630, Molecular Probes, Eugene, Oregon). Alexa Fluor® 488 wheat germ agglutinin was used to label elements of the glomeruli and convoluted tubules. The filamentous actin prevalent in glomeruli and the brush border were stained with red-fluorescent Alexa Fluor® 568 phalloidin. Finally, the nuclei were counterstained with the blue-fluorescent DNA stain DAPI. The excitation wavelength was 780 nm, the laser power per focus was about 6 mW, and the dwell time was 40 μs. The scanning size of one focus was 85 μm × 85 μm with 0.4 μm resolution, and the whole FOV was 680 μm × 680 μm for 8 × 8 foci. The excitation wavelength for the single focus scaning was the same 780 nm, the laser power was about 10 mW, and the dwell time was 40 μs. The scan size was also the same 680 μm × 680 μm with 0.5 μm resolution. Emission signals were collected without spectral separation for all three fluorophores.

Figure 7 shows the mouse kidney images taken in the descanned MMM, non-descanned MMM, and the standard single focus scanning microscope. Fig 7(a)-7(c) shows the raw images acquired from the three systems. For uniform signal intensity over the full FOV, the three raw mouse kidney images were normalized with the fluorescein solution images (Fig 7(g)-7(i)) acquired in each system with the same imaging condition as described in Section III A. The final processed non-descanned MMM image (Fig 7(d)) shows that the most of the objective lens FOV can be readily utilized, whereas the descanned MMM (Fig 7(e)) had a more limited FOV. The central region of both images showed similar SNR but signal attenuation in the radial direction was much more severe in the descanned MMM. A quantitative comparison is shown in Fig 8. From a FOV radial location of approximately 300 μm the descanned MMM showed no signal. In contrast, the non-descanned MMM showed emission signals up to the full field size. This signal attenuation of the descanned MMM is due to increasing aberrations at the image edge and the subsequent reduction in two-photon excitation efficiency. The non-descanned MMM showed about half the signal level of the single focus image. This lower signal is mainly due to the non-uniformity of the DOE. The power of the corner beamlet is about 70 % of the center beamlet, which is within its specification (target uniformity of all beamlets: ±15 %). Therefore, inherently the two-photon excitation of the corner focus has only half of the efficiency of the center focus. Due to the non-uniformity of the DOE and the aberrations from the intermediate optics the signal of the non-descanned MMM was lower than the single focus image. However, the non-descanned MMM could image the whole FOV 16 times faster (5 seconds of the non-descanned MMM excluding the manual sample movement time versus 77 seconds of the single focus scanning with the same number of pixels and same pixel size). In addition, it should be noted that the speed improvement can be eventually increased to 64 times while maintaining comparable SNR as described in Section E.

C. Signal attenuation comparison

We then proceeded to compare the signal collection efficiency between the descanned and non-descanned MMM in turbid medium. Fat emulsion (Microlipid, Nestle, Vevey, Switzerland) was added to the 300 μM fluorescein solution at 2% concentration same as in section III A. Images were acquired as a function of imaging depths at every 10 μm. Fig 9 shows the signal attenuation in the non-descanned (red) and descanned (blue) MMM. The power of the excitation laser in both systems was adjusted to be the same under the objective lens. To avoid the non-uniformity of the excitation

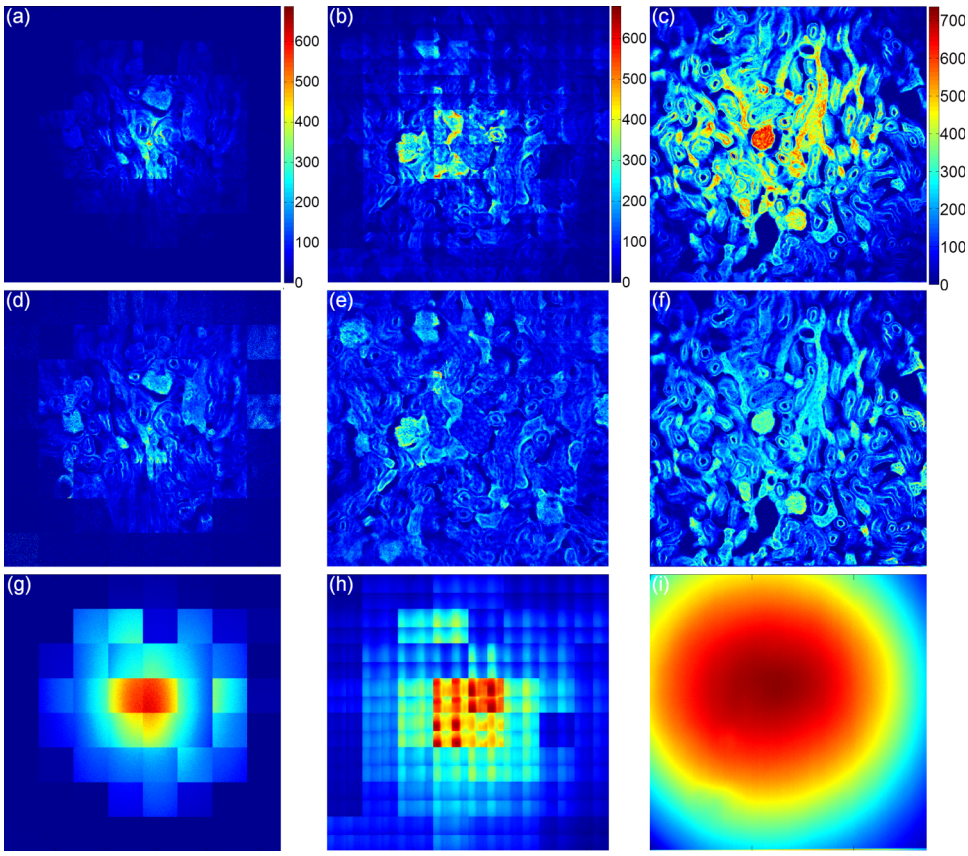

FIG. 7. Mouse kidney image. (a) Raw image of the descanned MMM, image size: 680 μm × 680 μm with 8 × 8 foci. (b) Raw image of the non-descanned MMM image with the same FOV with the same number of foci. (c) Raw image of the single focus scanning with the same FOV. (d-f) Normalized images of (a-c) with (g-i). (g-i) 20 times averaged fluorescein solution image of each system. The periodic pattern in (h) is the actual shape of the faceplate in front of the cathod in the MAPMT.

over the scanning area described above, only the signal at the center area was analyzed in this measurement. With the same excitation laser power and dwell time, the signal of the non-descanned MMM was higher than that of the descanned MMM. This improvement was apparent even at the surface since the forward emission photons were also scattered backwards and collected more in the

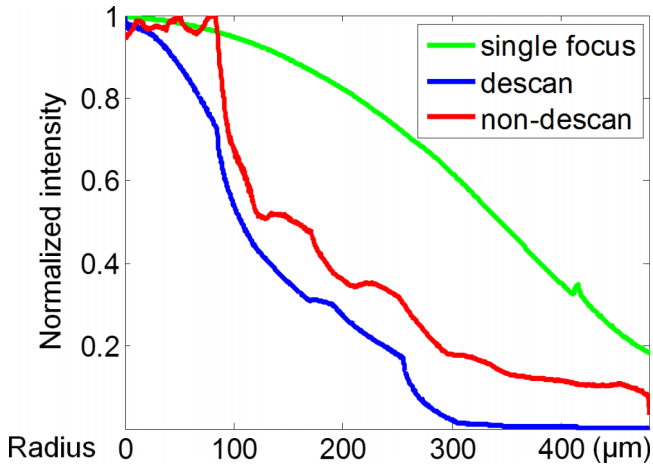

FIG. 8. Normalized intensity profile comparison of Fig 7(g)-7(i). The distance from the center to the corner of the 680 μm × 680 μm image is 481 μm.

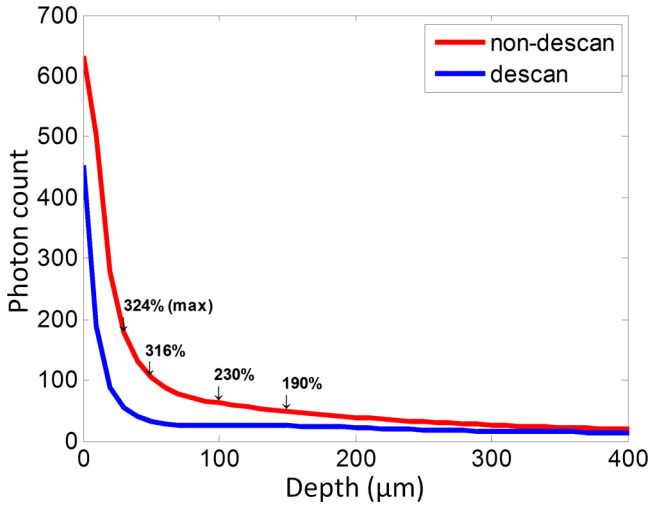

FIG. 9. Fluorescence emission signal attenuation in the descanned and non-descanned MMM. Data points are connected by lines for eye guidance.

non-descanned MMM with the shorter optical path and less optical components. The attenuation of the emission signal of the descanned MMM was much faster than the non-descanned MMM. For example, at 30 μm depth, the signal collection efficiency of the non-descanned MMM was three times higher than the descanned MMM. Up to about 150 μm depth, the signal improvement was observed about two-fold.

D. Mouse brain images with 4 × 4 MMM

We further tested the use of non-descanned MMM in a thick biological specimen. A Thy1-GFP transgenic mouse[31] was deeply anesthetized with 2.5% Avertin (0.025 ml/g i.p.) and transcardially perfused with PBS, followed by 4% paraformaldehyde. Its brain was dissected and postfixed overnight in cold 4% paraformaldehyde. 300 μm thick coronal sections were sectioned with a vibratome, then mounted and coverslipped on microscope slides using adhesive isolators. To excite the GFP efficiently, the excitation laser wavelength was adjusted to 910 nm. In the previous results the laser power at 780 nm was enough to generate 8 × 8 excitation foci, but the available laser power at 910 nm from the Ti-Sapphire laser was about one third of the power at 780m. Therefore, in this case 4 × 4 foci were generated with the same foci separation, and the total imaging size was 340 μm × 340 μm. The excitation laser power was approximately 35 mW per each excitation focus.

Figure 10 compares mouse brain images taken in the descanned MMM, non-descanned MMM, and the standard single focus scanning microscope at 40, 100, and 160 μm imaging depths. For uniform signal intensity, all the images were normalized with the fluorescein solution images acquired in each system with the same imaging condition described above. The imaging size was 340 μm × 340 μm with 4 × 4 foci (previously 680 μm × 680 μm with 8 × 8 foci). For the smaller FOV, the descanned MMM did not show significant signal loss at the image edge as the mouse kidney images. However, the non-descanned MMM could collect more emission signals as confirmed in section III C, and shows more structural details at the 160 μm depth. Comparing the non-descanned MMM images and the single focus scanned images, the single focus scanned images showed higher SNR as shown in section III B. However, the acquisition of the non-descanned MMM is 4 times faster than the single focus scanning reducing the 1~2 hour imaging time of some neurobiology experiments.[32,33] to 15~30 minutes, and possibly 4~8 minutes with further improvements that reduce scan time, while maintaining SNR as described in section II E. As a quantitative comparison of signal attenuation between the descanned and non-descanned MMM, the intensity trend of the neuronal cell bodies is plotted as a function of the imaging depth in Fig 11. For accurate comparison, only the brightest center parts of the cell bodies were counted. With the same

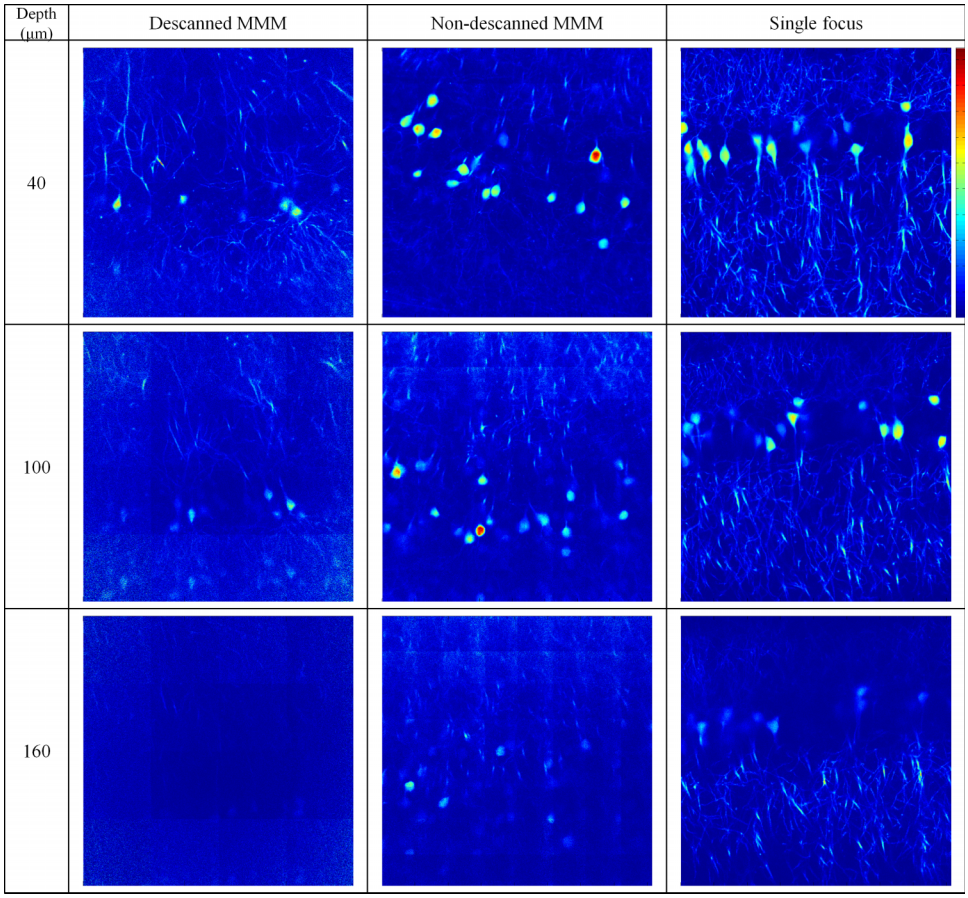

FIG. 10. Mouse brain images at 40, 100, and 160 μm depths. All images are 340 μm×340 μm with 0.4 μm pixel size. The left column images are descanned MMM images with 4 × 4 foci. The middle column images are non-descanned MMM images with 4 × 4 foci and the 4 time sample movement. The right column images are the standard single focus scanned images.

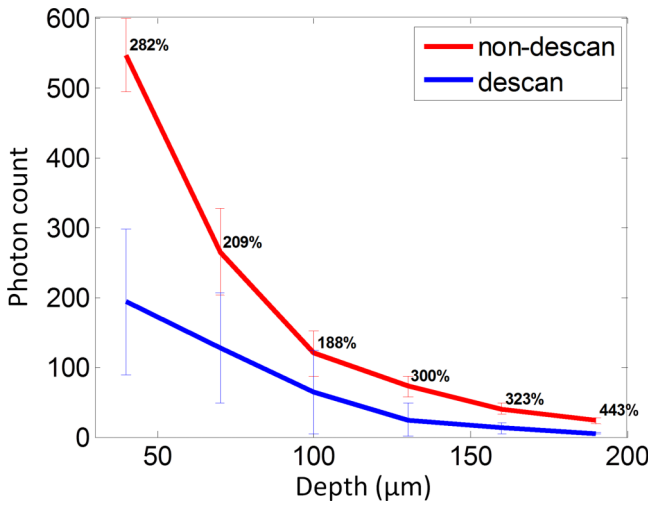

FIG. 11. The fluorescence emission signal attenuation of the neuronal cell bodies in the descanned and non-descanned MMM. The percentage numbers show the signal improvement, and the error bars show ± one standard deviation at each data point. The data points are connected by lines for eye guidance. Percentage values indicate the relative increase of the signal of the non-descanned image to the descanned image at the same depth.

excitation laser power and dwell time, the signal of the non-descanned MMM was higher than that of the descanned MMM as shown in Section C. The signal improvement was about two- to four-fold across the imaging depths.

IV. DISCUSSION AND CONCLUSION

The descanned MMM using the MAPMT can achieve better SNR compared to the traditional MMM by suppressing SNR degradation due to emission photon scattering. However, descanned detection still produces image artifacts, appearing as ghost sub-images due to channel crosstalk, and significant emission signal loss due to the long detection path length. The non-descanned MMM can minimize these ghost images by maximizing foci separation by fully utilizing the FOV of the objective lens with minimal aberrations for corner and edge foci. In addition, the non-descanned MMM can minimize the detection path length so that the signal collection efficiency can be improved up to four-fold. However, the emission signals are no longer stationary on the detector due to scanning, and a new detection scheme is necessary. We introduced a detection scheme of shifting a specimen and imaging four times. With four time acquisition of the emission signals by locating the specimen at the corresponding quadrant of one image, the non-stationary signals could be collected with avoiding the dead space of the MAPMT. Further, improvement of imaging speed using a larger number of foci can be achieved with high performance scanners and stage while obtaining comparable SNR to single focus scanning.

In addition to shifting the specimen and imaging multiple times, another potential approach to overcome the problem of MAPMT dead spaces in non-descanned mode is the use of multiple MAPMT detectors and projecting the image FOV slightly spatially displaced on the cathodes of these MAPMTs. The displacement scheme is similar to the specimen displacement approach described earlier (Fig 5); a minimum of three MAPMTs are needed but four can be used to improve final image SNR uniformity. Both specimen displacement and multiple MAPMT approaches have a similar final SNR. The advantage of using multiple MAPMTs is that image acquisition is done in a single scan and the result is immune to specimen motion artifacts. However, implementing multiple MAPMTs requires substantial more complex electronics, e.g. 256 acquisition channels for four 8×8 anode MAPMTs. Another possible option to circumvent MAPMT dead spaces would be the use of a custom parabolic light collector array that has minimal dead space between elements at the entrance and can funnel the emission photons reaching each element to the center area of a corresponding MAPMT anode. The custom parabolic light collector (CPC) array may be the best solution and will allow the single shot imaging with one MAPMT. However, the CPC should be fabricated with high precision such that the inlet size of the CPC exactly matches the anode matrix size of the MAPMT. The trade-off in the use of CPC is the more pronounced crosstalk between anodes requiring a more effective image post processing algorithm.

In any case, the standard single focus scanning two-photon microscope can often achieve better SNR than the MMM especially in great depth. However, there are many applications with bright specimens providing adequate SNR but where minimizing the acquisition time is critical. In this case, MMM can be a more desirable imaging solution, and the non-descanned MMM can perform better, with higher SNR and less crosstalk, while maintaining a larger FOV as compared with the previous version of descanned MMM.

ACKNOWLEDGMENTS

This research was supported by grant RO1 EY017656, NIH 9P41EB015871, 5 R01 NS051320, 4R44EB012415, NSF CBET-0939511, the Singapore-MIT Alliance 2, the MIT SkolTech initiative, the Hamamatsu Corp., and the Koch Institute for Integrative Cancer Research Bridge Project Initiative.

[1] W. Denk, J. H. Strickler, and W. W. Webb, Science **248**(4951), 73-76 (1990).
[2] P. T. C. So, C. Y. Dong, B. R. Masters, and K. M. Berland, Annual Review of Biomedical Engineering **2**, 399-429 (2000).
[3] K. H. Kim, C. Buehler, and P. T. C. So, Applied Optics **38**(28), 6004-6009 (1999).

[4] G. Fan, H. Fujisaki, A. Miyawaki, R. K. Tsay, R. Y. Tsien, and M. H. Ellisman, Biophysical Journal **76**(5), 2412-2420 (1999).
[5] V. Iyer, B. E. Losavio, and P. Saggau, Journal of Biomedical Optics **8**, 460 (2003).
[6] G. D. Reddy and P. Saggau, Journal of Biomedical Optics **10**, 064038 (2005).
[7] S. Zeng, X. Lv, C. Zhan, W. R. Chen, W. Xiong, S. L. Jacques, and Q. Luo, Optics Letters **31**(8), 1091-1093 (2006).
[8] G. Katona, G. Szalay, P. Maák, A. Kaszás, M. Veress, D. Hillier, B. Chiovini, E. S. Vizi, B. Roska, and B. Rózsa, Nature Methods **9**(2), 201-208 (2012).
[9] W. R. Zipfel, R. M. Williams, and W. W. Webb, Nature Biotechnology **21**(11), 1369-1377 (2003).
[10] G. C. Cianci, J. Wu, and K. M. Berland, Microscopy Research and Technique **64**(2), 135-141 (2004).
[11] D. Oron, E. Tal, and Y. Silberberg, Optics Express **13**(5), 1468-1476 (2005).
[12] G. H. Zhu, J. van Howe, M. Durst, W. Zipfel, and C. Xu, Optics Express **13**(6), 2153-2159 (2005).
[13] J. Bewersdorf, R. Pick, and S. W. Hell, Optics Letters **23**(9), 655-657 (1998).
[14] A. H. Buist, M. Muller, J. Squier, and G. J. Brakenhoff, Journal of Microscopy-Oxford **192**, 217-226 (1998).
[15] L. Sacconi, E. Froner, R. Antolini, M. Taghizadeh, A. Choudhury, and F. Pavone, Optics Letters **28**(20), 1918-1920 (2003).
[16] B. O. Watson, V. Nikolenko, and R. Yuste, Frontiers in Neural Circuits **3** (2009).
[17] K. H. Kim, C. Buehler, K. Bahlmann, T. Ragan, W. C. A. Lee, E. Nedivi, E. L. Heffer, S. Fantini, and P. T. C. So, Optics Express **15**(18), 11658-11678 (2007).
[18] J. Martini, V. Andresen, and D. Anselmetti, Journal of Biomedical Optics **12**(3), 034010-034010-034016 (2007).
[19] Y. Le Grand, A. Leray, T. Guilbert, and C. Odin, Optics Communications **281**(21), 5480-5486 (2008).
[20] J. P. Zinter and M. J. Levene, Optics Express **19**(16), 15348 (2011).
[21] M. Minsky, U.S. Patent No. 3013467 (19 December 1961).
[22] C. Sheppard and A. Choudhury, Journal of Modern Optics **24**(10), 1051-1073 (1977).
[23] G. Brakenhoff, P. Blom, and P. Barends, Journal of Microscopy **117**(2), 219-232 (1979).
[24] K. Carlsson and N. Åslund, Applied Optics **26**(16), 3232-3238 (1987).
[25] J. Pawley, *Handbook of biological confocal microscopy* (Springer, 2006).
[26] R. E. Fischer, B. Tadic-Galeb, P. R. Yoder, and R. Galeb, (2000).
[27] "Lens Selection Guide," in THE NEWPORT RESOURCE.
[28] "Multianode Photomultiplier Tube Assembly H7546A, H7546B," (HAMAMATSU).
[29] A. K. Dunn, V. P. Wallace, M. Coleno, M. W. Berns, and B. J. Tromberg, Applied Optics **39**(7), 1194-1201 (2000).
[30] C.-Y. Dong, K. Koenig, and P. So, Journal of Biomedical Optics **8**(3), 450-459 (2003).
[31] G. Feng, R. H. Mellor, M. Bernstein, C. Keller-Peck, Q. T. Nguyen, M. Wallace, J. M. Nerbonne, J. W. Lichtman, and J. R. Sanes, Neuron **28**(1), 41-51 (2000).
[32] J. L. Chen, W. C. Lin, J. W. Cha, P. T. So, Y. Kubota, and E. Nedivi, Nature Neuroscience **14**(5), 587-594 (2011).
[33] J. L. Chen, K. L. Villa, J. W. Cha, P. T. So, Y. Kubota, and E. Nedivi, Neuron **74**(2), 361-373 (2012).